

Polymer-Regulated Electrochemical Reduction of CO₂ on Ag

Ally Guo, Avery E. Baumann, Eric D. Rus, Christopher M. Stafford, and David Raciti*



Cite This: *J. Phys. Chem. C* 2023, 127, 17355–17365



Read Online

ACCESS |



Metrics & More

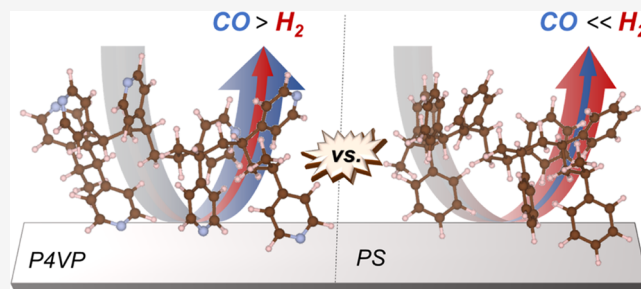


Article Recommendations



Supporting Information

ABSTRACT: The influence of polymer overlayers on the catalytic activity of Ag for electrochemical CO₂ reduction to CO is explored. Polystyrene and poly(4-vinylpyridine) films of varying thicknesses are applied as catalysis-directing overlayers atop Ag electrodes. For polystyrene, substantial suppression of CO₂ reduction activity is observed while the hydrogen evolution reaction (HER) increases. The addition of a nitrogen heteroatom into the phenyl groups of polystyrene (e.g., a pyridine ring) results in an increase in the conversion of CO₂ to CO and suppression of HER. Block copolymer variants containing both phenyl and pyridyl functionalities exhibit similar activity for CO evolution but appear to suppress HER further than the polymer layer containing only pyridine groups. The size of the blocks for the copolymer influences the catalytic output of the Ag electrode, suggesting that the hierarchical structure that forms in the block copolymer layer plays a role in catalytic activity at the electrode surface. Analysis of the polymer overlayers suggests that polystyrene significantly inhibits all ion transport to the metal electrode, while poly(4-vinylpyridine) enables CO₂ transport while modifying the electronics of the Ag active site. Therefore, the engineered application of polymer overlayers, especially those containing heteroatoms, enables new avenues of electrochemical CO₂ reduction to be explored.



INTRODUCTION

As of 2019, the annual global CO₂ emissions have surpassed 40 Gt/year, and while some regions of the world have improved to negative or near-zero emission growth rates, others have increased in emission growth rate.¹ Continued advances in CO₂ mitigation strategies including the electrochemical conversion of CO₂ to specialty chemicals or fuels are crucial to close the carbon cycle and invert the continuing emission trend. In order for the electrochemical CO₂ reduction reaction (eCO₂RR) to become a commercially successful strategy for alleviating CO₂ emissions, a salient understanding of the events occurring at the catalyst interface is essential. In this vein, substantial research has gone toward understanding the numerous reaction pathways of the eCO₂RR on bare metal surfaces.^{2,3} While pristine electrode surfaces serve the critical role of building a foundation of understanding in the laboratory, such electrodes are not representative of those used in commercial systems. Without considering the potential complexity in the chemical makeup of CO₂ feedstocks (e.g., trace amounts of hydrocarbons), high-surface-area catalysts developed for high durability and reaction rates are typically produced by using a variety of third-party additives.^{2,4,5} Of these strategies, molecules containing polar organic functional groups and even polymeric materials are a cornerstone and of late have been shown to have a critical influence over the activity and selectivity of metal catalysts for the eCO₂RR.^{6–24}

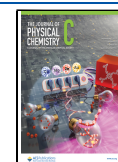
The intentional functionalization of catalytic surfaces with selectivity-modifying organic molecules has shown dramatic

improvement for the eCO₂RR. Functionalizing the metal catalyst surface with various bipyridyl derivatives had substantial effects on the conversion of CO₂ to C₂H₄ by tuning the ratio of adsorbed CO in atop vs bridge sites.^{20,25} Alternatively, various N-substituted pyridinium molecular additives have been investigated for their stereochemical effects on the eCO₂RR. In particular, para-substituted phenyl or tolyl variants electrochemically deposited on Cu surfaces resulted in activity and selectivity enhancement of CO₂ conversion to C₂₊ products (molecules with 2 or more carbon atoms), while a *tert*-butyl-substituted species enhanced the hydrogen evolution reaction (HER) instead.^{15,19} The use of pyridine has even been observed to steer CO₂ conversion toward methanol, among other influences, over the eCO₂RR.^{24,26–30} Another report similarly posits that the modulating distance of the functional group from the electrode surface significantly attenuates CO₂ conversion to CO on Ag surfaces with electrografted pyridine chains.⁸ These studies typically require an electrodeposition procedure to achieve their modified electrodes, a step that leads to the formation of heterogeneous films that can be chemically complex.

Received: May 12, 2023

Revised: July 13, 2023

Published: August 23, 2023



Conversely, polymers containing nitrogen heterocycles have shown promise in modulating the eCO₂RR when utilized as intact additives. The incorporation of a series of polyamines (and amine-less controls) during the electrochemical deposition of Cu onto gas diffusion layers indicated that the amine content correlated to a higher surface pH, higher CO coverages, and higher stabilization of intermediates. Under optimal conditions, the polyamine-incorporated Cu electrodes exhibited a 72% selectivity toward C₂H₄ with a total current density of 433 mA cm⁻² compared to 27% and 207 mA cm⁻² for bare Cu at -0.97 V vs the reversible hydrogen electrode (RHE) in 1 mol L⁻¹ of KOH.¹⁷ Similarly, Ag nanowires capped with polyvinylpyrrolidone initially suppressed the conversion of CO₂ to CO, but the suppression was overcome after going to potentials sufficiently negative to cause a change in the adsorbed polyvinylpyrrolidone structure.⁷ Functionalization of Cu, Au, and Pt with poly(4-vinylpyridine) (P4VP) was observed to increase the activity of the eCO₂RR, mainly in the production of formate, at substantially diminished overpotentials.^{12,13,31} Spectroscopic evidence demonstrated less adsorbed CO on the P4VP-covered Cu and a higher ratio of the dissolved CO₂ relative to HCO₃⁻ on P4VP-covered Au, suggesting inhibited mass transport of H₂O and HCO₃⁻.¹³ Aqueous mass transport effects were also supported through the modification of the hydrophilicity/hydrophobicity of the electrode interface with P4VP. Similar hydrophobicity effects were observed when alkanethiols were anchored to Cu dendrites.²³

As exemplified over the past several years, the combination of metal electrodes and functionalized polymers can provide new opportunities in the eCO₂RR through a variety of physical and chemical mechanisms. In this work, we investigated the role that polyvinyl derivative overlayers play in tuning the selectivity and activity of a textured Ag(111) thin film electrode for the eCO₂RR. The polymers studied exhibit a range of surface energies and vary in their ability to influence the electronic structure of the Ag surface, manifesting in our electrochemical results. Evaluation of block copolymers containing the same functionalities provides insight into the role that the hierarchical structure plays in these systems. The native catalytic behavior of an evaporated Ag(111) thin film produced a mixture of CO and H₂, favoring the hydrogen evolution reaction (HER). Application of a thin polystyrene overlayer resulted in the suppression of CO evolution and a substantial increase in the H₂ activity relative to that for an unmodified electrode, while thicker layers suppressed the activity of both reactions. Substitution of the phenyl group for a pyridyl functional group resulted in over 10 × enhancement in the CO production and 8 × suppression in HER. Furthermore, an electrode covered with a block copolymer of the two functional groups exhibits catalytic behavior distinct from unmodified Ag or Ag modified with either individual polymer. Characterization of these polymer overlayer electrodes demonstrates how the specific interaction of the pyridine functional group with the Ag surface plays an integral role in activating the electrocatalytic reduction of CO₂ to CO, while the hydrophobicity of the polymer likely attenuates the transport of aqueous species.

METHODS

Materials. Silicon wafers (orientation <100>, p-doped, test grade) were purchased from University Wafers*. Polymers used for film deposition consisted of poly(styrene) (PS, M_n =

8.8 kg mol⁻¹, M_n/M_w = 1.09, Polymer Source), poly(4-vinylpyridine) (P4VP, M_n = 8.8 kg, M_n/M_w = 1.11, Polymer Source), and poly(styrene-*b*-4-vinylpyridine) (PS-*b*-P4VP, “10k” M_n = 5-*b*-5 kg mol⁻¹, M_w/M_n = 1.18, Polymer Source; “40k” M_n = 21.4-*b*-20.7 kg mol⁻¹, M_w/M_n = 1.13, Polymer Source) and were used as received. M_n is the number-average molar mass, and M_w is the mass-average molar mass.

Evaporation of Ag Thin Films. Ag thin films were prepared using e-beam evaporation on 15 cm Si <100> wafers. First, the Si <100> wafer was rinsed with ethanol and dried with a stream of N₂. Then, the wafer was treated in an ultraviolet-ozone (UV-O) cleaner for 20 min. Afterward, the Si wafer was transported in a wafer carrier to the evaporation chamber. After mounting, the chamber was pumped to an ultrahigh vacuum overnight. With the wafer facing away from the deposition target, a 5 nm Ti prerun (≈1 Å s⁻¹) was performed to scrub any residual O₂ from the chamber. The amount deposited was monitored via two internal quartz crystal microbalances. Afterward, the wafer was rotated to face the Ti target and 5 nm of Ti (≈1 Å s⁻¹) was deposited onto the wafer surface to act as an adhesion layer for the Ag. The wafer was then rotated to face the Ag target, and 50 nm of Ag was deposited (≈1 Å s⁻¹). After deposition, the wafers were removed from the evaporation chamber and stored in a dry box until use.

X-ray Measurements. X-ray diffraction (XRD) and reflectivity measurements (XRR) were carried out using a Bruker D8 Advance Diffractometer employing Cu Kα X-rays, Montel optics, and a Dectris Eiger 2R 500K detector. XRD was measured in a $\theta/2\theta$ configuration. XRR data were fit with Refl1D.

Preparation of Ag-Polymer Composite Electrodes. Polymer-coated Ag electrodes were prepared via spin coating. Prior to spin coating, solutions of poly(4-vinylpyridine), polystyrene (PS), and poly(styrene-*b*-4-vinylpyridine) (PS-*b*-P4VP) were prepared at varying concentrations from 2 mg mL⁻¹ to 10 mg mL⁻¹ in ethanol, toluene, and tetrahydrofuran, respectively. Solvents were filtered prior to use. First, Ag-coated silicon substrates were mounted on the vacuum chuck of the spin coater (Headway, Model EC101) and rinsed with ethanol before spinning dry at 4000 rpm (419 rad s⁻¹). Next, dilute polymer solutions were dispensed onto cleaned Ag-coated silicon substrates and then spun immediately at 4000 rpm for ≈30 s. Electrodes were cleaned by first rinsing with ethanol, drying with N₂, and, when indicated, exposing to UV-ozone for 2 min before use.

Atomic Force Microscopy. Atomic force microscopy (AFM) measurements were performed using a Bruker Dimension Icon AFM operating in tapping mode and using an RTESPA-300 cantilever (resonant frequency = 300 kHz, spring constant = 40 N m⁻¹, nominal tip radius = 8 nm). Images (5 mm × 5 mm) were collected at a scan rate of 1.0 Hz, and the root-mean-square roughness (R_q) was calculated using the NanoScope Analysis software.

Ellipsometry. The thickness of the polymer layer was characterized via variable angle spectroscopic ellipsometry (VASE, M-2000XI, J.A. Woollam). Spectra were obtained at incidence angles in the range of 50–70° in discrete increments of 10° and over a wavelength range of 210 nm to 1700 nm. Measurements were conducted at four points near the center of the substrate to minimize edge effects from the spin coating process. The unmodified Ag-coated substrate was measured first and fit to an optical model consisting of silicon, native

silicon oxide, Ag, and Ag oxide. Based on these measurements, we were able to fix the optical properties of the Ag-coated substrates (prior to depositing polymer films) as a semi-infinite Si substrate, $\text{SiO}_x = 1.7$ nm, $\text{Ag} = 49.87$ nm, and $\text{AgO}_x = 1.63$ nm. The Ag layer was fit to a B-spline model. The optical constants for PS, P4VP, and PS-*b*-P4VP were obtained from fitted values of films spin-coated onto silicon wafers and modeled as a Cauchy layer (eq 1) on silicon with a native oxide (1.7 nm). The model coefficients were determined to be $A = 1.52$ and $B = 0.013$ for PS, $A = 1.55$ and $B = 0.014$ for P4VP, $A = 1.55$ and $B = 0.0073$ for 10k PS-*b*-P4VP, and $A = 1.53$ and $B = 0.0078$ for 40k PS-*b*-P4VP. These coefficients were then fixed when fitting the polymer films spin-coated onto Ag-coated substrates, such that the only fitting parameter in the optical model was the polymer film thickness. The data fitting was restricted to (300–1600) nm due to the absorption of phenyl rings around 254 nm

$$n(\lambda) = A + \frac{B}{\lambda^2} \quad (1)$$

Electrochemical CO₂ Reduction Experiments. Evaluation of the Ag–polymer composite electrodes for the eCO₂RR was performed in a custom H-cell, similar to a previously reported configuration, using 0.1 mol L⁻¹ of KHCO₃ as the electrolyte.^{32,33} 0.1 mol L⁻¹ of KHCO₃ was prepared via sparging of a 0.05 mol L⁻¹ K₂CO₃ solution with 20 mL min⁻¹ of CO₂ overnight. The pH the following day was measured to be 6.8, typical for a CO₂-saturated 0.1 mol L⁻¹ KHCO₃. A ≈ 2 cm × ≈ 2 cm electrode was pressed against the cathode chamber's backplate with a polytetrafluoroethylene gasket. The exposed electrode area was 2 cm² (via a hole in the backplate with ≈1.6 cm diameter). The cathode compartment (≈12 mL volume, 2 mL gas headspace) was separated from the anode compartment using an anion-exchange membrane (Fumasep FAA-PK-130). This membrane was stored in 1 mol L⁻¹ of KOH prior to use. The anode, a ≈6 cm² Pt gauze, was hung via a Pt wire in the 10 mL anode compartment. A double junction Hg/HgSO₄ reference electrode saturated with potassium sulfate was used for all electrochemical experiments. For all measurements involving CO₂, the 0.1 mol L⁻¹ KHCO₃ was prepurged with CO₂ overnight and a 20 mL min⁻¹ flow rate was pumped through a 40 μm to 60 μm porous glass frit submerged in the cathode compartment's electrolyte during the experiment. Potentials from -0.7 V to -1.1 V vs the reversible hydrogen electrode (RHE to be assumed throughout) were applied in -0.1 V increments sequentially for 30 min with the same electrode unless otherwise indicated. Electrochemical measurements were performed using an Autolab 204N potentiostat (Metrohm). A gas chromatograph (SRI, Inc. Multigas Analyzer #5) equipped with a thermal conductivity detector (TCD) and flame ionization detector (FID) was used to evaluate the cathode gas flow starting at 3 min and every 5 min afterward. Ar was used as the carrier gas to allow for the quantification of H₂. A few mL of electrolyte were collected for liquid product analysis via nuclear magnetic resonance (NMR) spectroscopy at the end of every 30 min potential step, and the electrolyte was refreshed before the start of a new potential. All potentials discussed in this work were converted to the RHE scale using the Nernst equation

$$E(\text{vs RHE}) = E(\text{vs Hg/HgSO}_4) + 0.64 \text{ V} + 0.0591 \times \text{pH} \quad (2)$$

The resistance between the cathode and reference electrode was measured using the current-interrupt method of the Autolab potentiostat prior to each measurement.³⁴

Faradaic efficiencies and partial geometric current densities for gas products were calculated using the following two equations, respectively

$$\text{FE}\%_x = \frac{\text{ppm} \times q_{\text{gas}} \times \frac{nFp_o}{RT}}{J_{\text{Tot}}} \times 100 \quad (3)$$

$$J_{x,\text{geo}} = \frac{\text{ppm} \times q_{\text{gas}} \times \frac{nFp_o}{RT}}{\text{geometric surface area}} \quad (4)$$

where ppm is the concentration of the analyte in parts per million ($\text{ppm} = \mu\text{g kg}^{-1}$), q_{gas} (L s⁻¹) is the gas flow rate, n is the number of electrons transferred, F is Faraday's constant, R (L atm mol⁻¹ K⁻¹) is the gas constant, p_o is atmospheric pressure (atm), T (K) is the ambient temperature, and J_{Tot} is the total current (A) measured for a given potential.

Solution NMR Measurements. Liquid products were monitored via solution NMR on a 600 MHz spectrometer. 0.665 mL of a given liquid sample was injected into an economy grade 5 mm diameter, 7 inch long 600 MHz NMR tube, followed by 70 μL of 5 mmol L⁻¹ dimethyl sulfoxide (DMSO) in D₂O. The DMSO served as an internal standard for the quantification of liquid products, while deuterium served as the locking substance. Measurements were performed using a 5 mm broad-band observe (bbo) probe with a 4 scan delay, a 10.09 degree read-pulse, and over 8278 Hz spectral width for 64 scans with water suppression. A linear regression through standard solutions was used to determine the concentration of analyte samples as demonstrated previously.³² Faradaic efficiency and partial geometric current density for liquid products were calculated via the following equations

$$\text{FE}\%_x = \frac{nMVF}{tJ_{\text{Tot}}} \times 100 \quad (5)$$

$$J_{x,\text{geo}} = \frac{nMVF}{\text{geometric surface area}} \quad (6)$$

where M is the concentration (mol L⁻¹) of the liquid product from the electrolyte aliquot obtained from the experiment, V (L) is the volume of the catholyte, and t (s) is the duration of the applied potential.

X-ray Photoelectron Spectroscopy Measurements. X-ray photoelectron spectroscopy (XPS) measurements were performed using a Kratos AXIS Ultra DLD spectrometer (Kratos Analytical, Manchester, U.K.) with a monochromatic Al K_α source (1486.6 eV) operating at 140 W. The base pressure of the sample analysis chamber was ≈1.0 × 10⁻⁹ Torr (≈1.33 × 10⁻⁷ Pa), and spectra were collected from a nominal spot size of 300 μm × 700 μm. Measurements were performed in hybrid mode using electrostatic and magnetic lenses, and the pass energy of the analyzer was set at 160 eV for survey scans and 20 eV for high-resolution scans with energy resolutions of 0.5 eV and 0.1 eV, respectively. All XPS data analyses were performed using the CasaXPS software package, and peaks were fit using the Tougaard analysis.

Contact Angle Measurements. A 7.6 μL water droplet was dispensed onto the thin film surface with a syringe. The static contact angle was measured with a drop shape analyzer

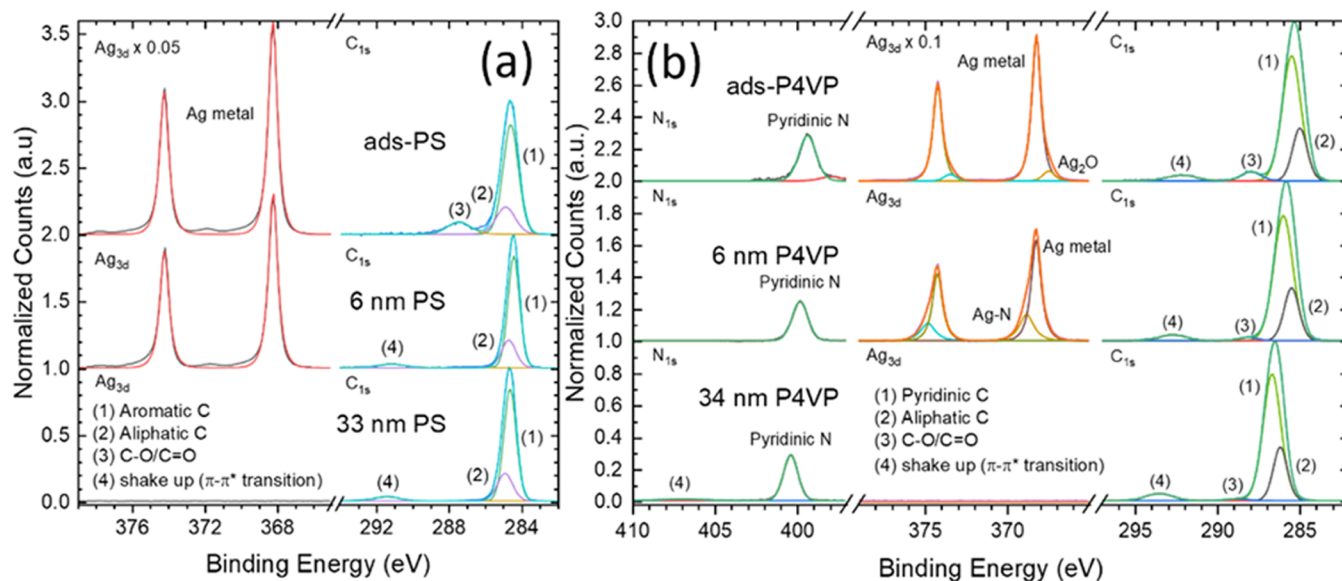


Figure 1. XPS measurements of the Ag thin film with (a) PS and (b) P4VP polymer overlayers of different thicknesses on Ag thin films.

(Kruss) and modeled using the Young–Laplace fitting method with a fitted baseline.³⁵

Electrochemical Impedance Spectroscopy. Electrochemical impedance spectroscopy (EIS) measurements were conducted using the same H-cell configuration as the CO₂ reduction experiments using a BioLogic SP-300 potentiostat. The freeware “EIS Spectrum Analyzer” was used for equivalent circuit modeling.³⁶ Cyclic voltammetry, at multiple scan rates, in an Ar-purged 0.1 mol L⁻¹ KHCO₃ was used to determine a potential region with negligible faradaic processes in which to conduct EIS measurements. Ultimately, 0.58 V vs RHE was chosen for EIS measurements. For all measurements, the electrolyte was purged for ≈30 min at 20 mL min⁻¹ with Ar prior to and during measurements. All impedance measurements were from 0.1 Hz to 100 kHz with an AC amplitude of 10 mV and a 10 s quiet time with a sampling interval of 16 points per decade.

RESULTS AND DISCUSSION

Polymer overlayers were deposited onto the 50 nm (111)-textured Ag thin film (see the Supporting Information section Ag(111) Thin Film Electrode Characterization and Figures S1–S5), analyzed for their influence on the eCO₂RR and characterized using XPS (Figure 1). The homopolymers examined in this study (PS and P4VP) were practical as they were (i) not soluble in the electrolyte solution, (ii) amenable to common casting procedures (i.e., spin/dip casting), and (iii) widely commercially available. Two strategies were used to prepare the PS and P4VP overlayers. First, to achieve a surface-adsorbed thickness, e.g., nominally only a specifically adsorbed layer of polymer, samples were submerged in polymer solution for 15 min and then submerged in a fresh solvent in the absence of polymer, before gently being rinsed in the appropriate solvent. These samples are referred to as “ads-polymer” (e.g., PS or P4VP). For thicker samples, 0.2 wt % and 1 wt % solutions (percent by mass = mass fraction × 100) were deposited onto the Ag thin film via spin coating at 4000 RPM for 30 s (more details are available in the Methods section). In the case of block copolymer variants, 10k and 40k PS-*b*-P4VP, only 0.2 wt % was used to prepare overlayers. Ellipsometry

measurements were used to measure the thickness of the resulting polymer overlayers, while AFM was used to measure the variability in film roughness. A series of controls were used to ascertain appropriate constants (Tables S1 and S2) for fitting the ellipsometry to Cauchy’s equation (eq 1) (see the Methods section). The ellipsometry measurements on Ag are in good agreement with the reflectometry with a metal thickness near 50 nm, while both P4VP and PS had thicknesses of ≈6 nm and ≈33 nm to 34 nm for 0.2 wt % and 1 wt %, respectively (Table 1). In the case of 10k PS-*b*-P4VP and 40k

Table 1. Polymer Overlayer Thicknesses on Ag Thin Films Determined by Ellipsometry Using Cauchy’s Equation^a

polymer solution	A	B	polymer thickness (nm)
0.2 wt % PS	1.52	0.013	5.8 ± 0.1
1 wt % PS	1.52	0.013	33.0 ± 0.1
0.2 wt % P4VP	1.55	0.014	6.2 ± 0.1
1 wt % P4VP	1.55	0.014	33.8 ± 0.1
0.2 wt % 10k PS- <i>b</i> -P4VP	1.55	0.0073	15.6 ± 0.1
0.2 wt % 40k PS- <i>b</i> -P4VP	1.53	0.0078	21.5 ± 0.3

^aBold numbers were fixed for the fitting process and were determined via control ellipsometry measurements (see the Methods section for more details). The Si oxide, Ag, and Ag oxide thicknesses were fixed for each sample at 1.7 nm, 49.87 nm, and 1.63 nm, respectively.

PS-*b*-P4VP block copolymers, the thicknesses were measured to be 15.6 nm ± 0.1 nm and 21.5 nm ± 0.3 nm, respectively. AFM images (Figures S6–S8) demonstrate that uniform polymer films were produced via the spin coating process. In fact, the original Ag surface has the largest RMS roughness (≈2.6 nm when averaging both surfaces in Figure S3), and as the polymer film thickness increases, the RMS roughness decreases for PS and P4VP films (1.76 nm being the highest and 0.502 nm being the lowest). The PS-*b*-P4VP films appear to have a higher RMS roughness for their thickness, especially the 20k block, which has an RMS roughness of 1.4 nm (Figure S7).³⁷

With surface-adsorbed samples being too thin to measure with ellipsometry, XPS was used to qualitatively compare the polymer content between samples. The intensity of the Ag

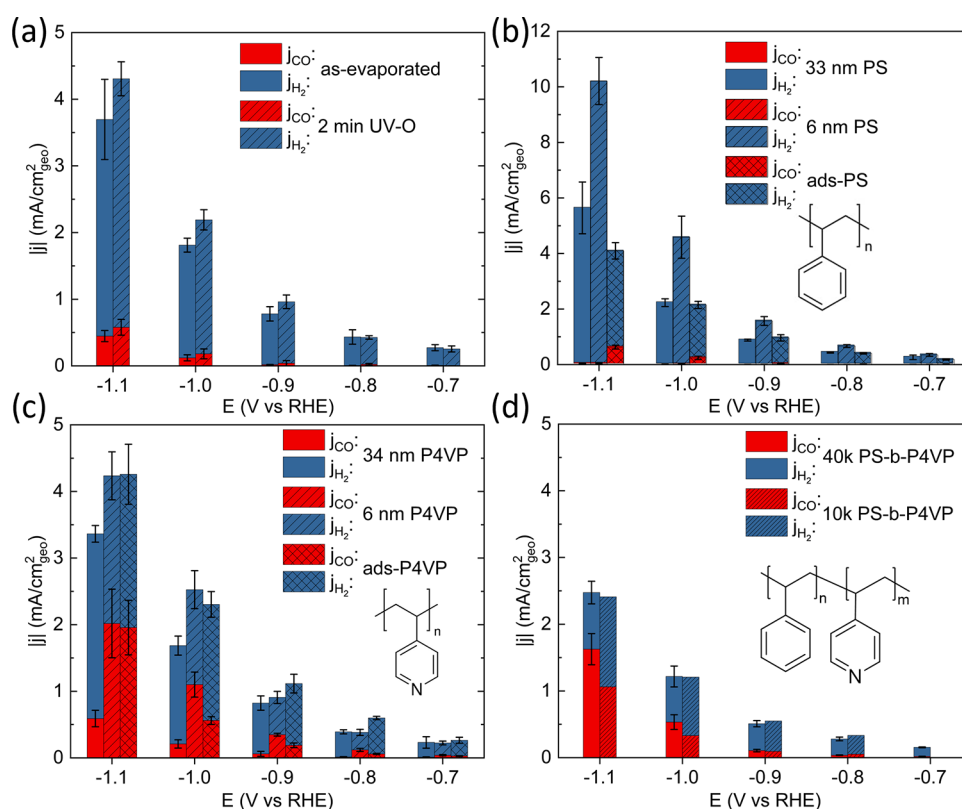


Figure 2. eCO₂RR on as-evaporated Ag, UV–O-treated Ag, and Ag with polymer overlayers. Geometric current densities (stacked) for H₂ and CO on (a) as-evaporated Ag, Ag treated with 2 min UV–O, and Ag with (b) P4VP, (c) PS, or (d) PS-*b*-P4VP block copolymer overlayers in a H-cell with 0.1 mol L⁻¹ of KHCO₃ as the electrolyte.

3d_{5/2} peak relative to the C_{1s} peak from XPS accurately captures the much thinner PS and P4VP layers formed for the adsorbed samples (Figures 1 and S9). The ads-PS sample demonstrated C–O/C=O functionality in the C_{1s}, likely from adventitious carbon still present on the surface after loading the polystyrene. Thicker PS layers only exhibited aromatic and aliphatic carbon typical of a polystyrene standard spectrum (Figure S10a), which was used for fitting polymer overlayer spectra.^{38,39} The 33 nm PS overlayer sample demonstrated no Ag_{3d} due to the relatively short inelastic mean free path of the emitted photoelectrons.

In the case of P4VP, the XPS not only enabled a comparison of the relative thicknesses but also revealed binding information between the N in the pyridine ring and Ag. XPS of molecular pyridine deposited on Ag demonstrates two peaks, at 398.9 eV and 401 eV, with the latter increasing substantially when thicker layers of pyridine were analyzed.⁴⁰ All samples show the primary peak for N_{1s} centered near 400 eV (Figure 1b), characteristic of bulk P4VP (Figure S10b,c), albeit with shifting, which may be due to issues with differential charging in the polymer since the spectra were shifted to Ag 3d_{5/2}.³⁹ However, the ads-P4VP sample, being the thinnest, demonstrates a subtle shoulder near 398 eV that reflects the coordination between N and Ag. In ads-P4VP, the Ag 3d_{5/2} peaks are predominantly bulk Ag metal with minor contributions from Ag₂O (not observed in other samples). Given the thin layer of P4VP, the photoelectrons detected from silver are likely comprised of several atomic layers, which may overshadow any shifts in Ag 3d_{5/2} peaks due to coordination with N. This finding is consistent with the aforementioned XPS study on molecular pyridine-coated Ag

(which was limited to ≤4 monolayers of pyridine atop the substrate) where no shift in the Ag_{3d} electron binding energies were observed.⁴⁰ Interestingly, for the 6 nm P4VP overlayer, the Ag 3d_{5/2} peak was comprised of two peaks, bulk metal at 368.2 eV and a smaller peak at 368.8 eV that has been previously attributed to surface Ag–N interactions.^{41,42} It is likely the photoelectrons detected from Ag will be confined to the metal surface given the thicker polymer layer, which may put emphasis on Ag atoms coordinated to N. This is supported by the much larger N_{1s} and C_{1s} peaks relative to the Ag 3d_{5/2} peak. The Ag substrates prepared with 15.6 nm 10k and 21.5 nm 40k PS-*b*-P4VP have more Ag–N character with higher intensities at 368.8 eV (Figure S11), with 40k PS-*b*-P4VP being the most pronounced. Identification of Ag_{3d} in samples prepared with PS-*b*-P4VP overlayers comes as a surprise given the thickness, but the slightly larger RMS roughness from AFM suggests that there could be local regions of thinner regions or possible pinholes that may allow for the respective photoelectrons to escape. A relative comparison between the C_{1s} and N_{1s} demonstrates the larger ratio of C to N (15:1) in the PS-*b*-P4VP overlayers vs the P4VP (7:1) (Figure S11 vs Figure 1).

eCO₂RR experiments (see the Methods section for details and Figure S12 for current vs time plots) on the evaporated Ag primarily produced H₂ (Figure 2a) with only minor amounts of CO being detected at potentials ≥ –0.9 V. The partial current density for CO increased to 0.5 mA cm_{geo}⁻², where “geo” refers to the geometric surface area of the catalyst instead of the electrochemical active surface area at potentials ≤ –1.0 V. In comparison, the partial current density for the HER was ≈3 mA cm_{geo}⁻², or an 84% current efficiency (Figure S13). The UV–O treatment did not seem to considerably modify

the selectivity of the Ag thin film but did increase the overall geometric current density as one would expect due to the increased roughness of the surface; thus, further substrates used to investigate the impact of polymer overlayers were not subject to UV–ozone treatments. Liquid product analysis (see the [Methods](#) section) was utilized to track the quantity of formate in the electrolyte for each potential studied; however, only small amounts, near the limit of detection of the instrument, equivalent to <5% current efficiency, were measured at -1.1 V ([Figure S14](#)).

The high HER selectivity observed for the (111)-textured Ag ≥ -1.1 V is congruent with previous reports.^{43,44} The textured evaporated film in this work demonstrates even higher selectivity for the HER compared to an epitaxially grown Ag(111) thin film (86% vs $\approx 50\%$ around -1 V, respectively), which could result from the increased H binding energy due to differences in stress that result from the evaporation process.^{44–47} Other reports have investigated the production of single-crystal-like surfaces using thin film fabrication procedures and obtained eCO₂RR results more in line with pure single-crystal counterparts.⁴⁴ Another possibility, besides stress induced by evaporation, could be the influence of ambient adventitious carbon on the surface. A previous study on polyvinylpyrrolidone-capped Ag nanowires demonstrated a hysteresis in H₂ and CO production that was dependent on the terminal potential studied.⁷ In essence, the catalyst favored the HER when stepping to more negative potentials from -0.6 V with the onset for CO₂ conversion to CO not occurring until -0.9 V. However, after reaching the most negative potential, CO became the dominant product, and when reverse stepping back to -0.6 V, it generally remained the dominant product. This hysteretic behavior or activation was assigned to a decrease and structural change of surface polyvinylpyrrolidone, detected via XPS, due to the formation of CO at more negative potentials that disrupted the bonding of O and N from the polymer to the Ag active sites. It was noted that when H₂ was the predominant product, the polyvinylpyrrolidone coverage did not decrease. To explore whether the adventitious carbon measured on the surface in the present work elicited a similar effect, the potential was stepped back to -0.6 from -1.1 V ([Figure S15a](#)) following the initial eCO₂RR experiment in [Figure 2a](#). The eCO₂RR activity was observed to be twice what was recorded for the initial chronoamperometry experiments at -0.9 and -1.0 V. At more positive potentials, eCO₂RR activity fell off and only HER was observed. Therefore, the measured catalytic properties of the surface likely reflect the nature of the Ag active sites with perhaps minute influence caused by ambient surface carbon.

For electrodes with polymer coatings, eCO₂RR experiments were conducted about 1 h after preparing the polymer layer. The ads-PS sample demonstrated very similar catalytic activity when compared to the unmodified Ag thin film with >80% selectivity for the HER at -1.1 V ([Figure 2b](#)). However, increasing the film thickness (6 nm PS) increased H₂ selectivity to >99% at all potentials investigated. Additionally, the geometric current density of H₂ increased substantially at all potentials, reaching ≈ 10 mA cm_{geo}⁻² at -1.1 V, almost 3 \times that observed for the unmodified Ag film. Further increasing the film thickness (33 nm PS) did not alter the dominant H₂ selectivity but did suppress the current density. Previous reports have noted that the adsorbed CO is responsible for the suppression of the HER.¹³ It is possible that ≥ 6 nm PS overlayers impede the transport of CO₂ to the surface,

lowering the steady-state coverage of CO chemisorbed on the Ag surface, thus resulting in greater HER current density. Linear scan voltammetry ([Figure S15b](#)) collected on bare Ag supports this notion. In an Ar-purged 0.1 mol/L KHCO₃, the total current density approaches -3 mA/cm² by -0.7 V. Purging the solution with CO₂ (while holding the potential at ≈ -0.1 V) and running another linear scan results in a substantially suppressed total current density congruent with the steady-state measurements shown in [Figure 1a](#). Presumably in the absence of CO₂, the dominant reaction is the HER; given the considerably higher current density at lower overpotentials, it is likely that the steady-state HER kinetics of bare Ag in Ar-saturated KHCO₃ will be considerably higher than observed for Ag with varying thicknesses of PS, supporting that PS also impedes the transport of HER reactants. In contrast to PS, both ads-P4VP and the 6 nm P4VP overlayer electrodes produce a substantial amount of CO from the eCO₂RR ([Figure 2c](#)). The ads-P4VP-covered Ag electrode shows slightly less CO activity at potentials above -1.1 V compared to the 6 nm P4VP film, but by -1.1 V, both ads and 6 nm P4VP-coated electrodes yield partial CO current densities of 2 mA cm_{geo}⁻². The 6 nm P4VP-covered Ag electrode also exhibited lower current densities toward the HER compared to the ads-P4VP electrode, but nominally both samples produced 2.2 mA cm_{geo}⁻² of H₂ by -1.1 V. Compared to unmodified Ag, partial CO current density was enhanced $\approx 4 \times$ with the 6 nm P4VP layer, whereas HER was suppressed ≈ 0.67 . This inhibition could be a result of the increased surface-adsorbed CO arising from alteration of the local Ag surface (via *N*-coordination) and local coordination sphere or attenuated proton transport to the surface of Ag. This inhibition could be a result of the increased surface-adsorbed CO or attenuated proton transport to the surface of Ag. Increasing the P4VP thickness further (34 nm P4VP) worsens selectivity for the eCO₂RR, resulting in higher H₂ activity at all potentials, compared to the thinner variants, with only about 0.68 mA cm_{geo}⁻² going toward CO and 2.72 mA cm⁻² toward H₂ at -1.1 V. Thicker layers of P4VP could begin to restrict charge transfer due to the suppressed electrolyte permeability.³¹

Introducing a symmetric block copolymer (see the [Methods](#) section for the number-average molar mass of each block) containing both PS and P4VP segments (PS-*b*-P4VP) allows the investigation of functional group competition, where the pyridyl or phenyl group has equal access to the electrode surface upon film casting. Catalytic activity of the PS-*b*-P4VP-coated electrodes more closely resembles those of P4VP than PS in both the eCO₂RR and HER ([Figure 2d](#)). The 10k and 40k PS-*b*-P4VP overlayer electrodes have lower overall geometric current densities in comparison to all other electrodes studied, reaching just 2.5 mA cm_{geo}⁻² by -1.1 V. However, they also generally demonstrate the lowest HER partial currents reaching just ≈ 1.35 mA cm⁻² and 0.85 mA cm⁻² by -1.1 V for the 10k and 40k PS-*b*-P4VP variants, respectively. The partial CO current density is suppressed relative to the thinner P4VP overlayer electrodes, where 40k PS-*b*-P4VP is only suppressed by 19%, while the 10k PS-*b*-P4VP is suppressed by 47%, opposite of what one may expect if the thickness was the cause behind the suppression (as observed for the 34 nm P4VP film). Thus, the 40k PS-*b*-P4VP maintains the highest current efficiency of 66% toward CO observed in this study. However, it should be noted that the ratio between N_{1s} and Ag_{3d} decreases substantially after

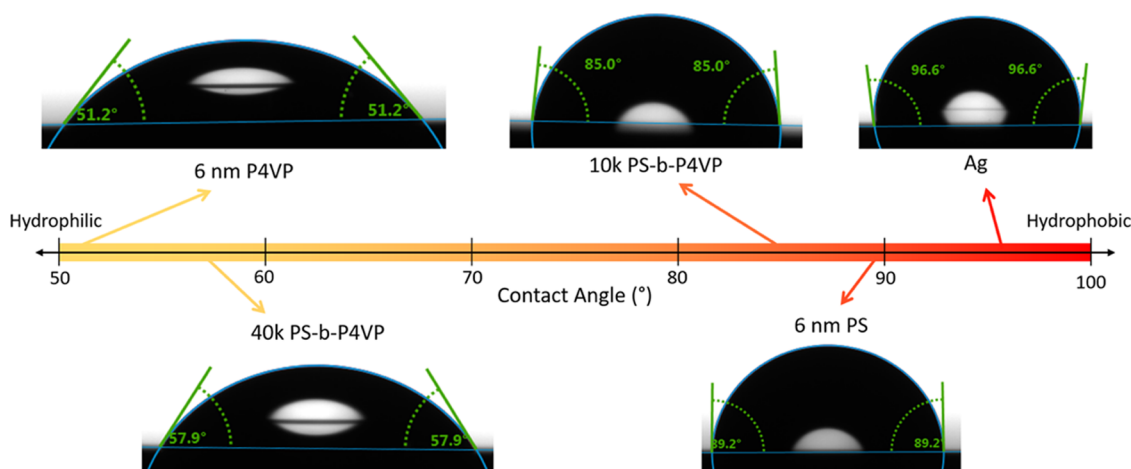


Figure 3. Contact angle measurements on the unmodified Ag and Ag with polymer overlayers.

eCO₂RR experiments on pyridine-containing overlayers, indicating that polymer is lost during electrolysis (Figure S16a). A subtle change in peak shape was also observed near 400 eV (Figure S16b–d) with the development of a small shoulder near 401 eV, which could show slightly different C–N interactions. Additionally, a peak near 407 eV was present for ads-P4VP and 6 nm P4VP overlayers, which may indicate O–N interactions; however, this peak did not appear to be present for the Ag electrode with a 34 nm P4VP polymer overlayer. Going back to the implication of polymer loss (e.g., loss in the N_{1s} peak area), one may expect to see an additional peak for Ag–N interactions as observed for ads-P4VP in Figure 1b. The absence of this peak implies that either Ag–N interactions break down during electrolysis or polymer loss is nonuniform. The latter is supported by the increased standard deviation around the average N_{1s}/Ag_{3d} ratio of three different locations of the electrode (Figure S16a) collected after eCO₂RR experiments. The current vs time plots (Figure S12) do not demonstrate substantial changes over the course of each potential, suggesting that this could occur at low overpotentials before substantial differences in catalytic activity have occurred or perhaps during electrolyte changes. With the exception to ads-P4VP, it appears that the pyridine-containing polymer electrodes all drop to similar N content relative to Ag. Given that the block copolymers also contain polystyrene chains, the equivalent N_{1s}/Ag_{3d} ratio suggests more total polymer content for the PS-*b*-P4VP overlayers. This increased polymer content as well as the observed selectivity differences in the eCO₂RR for PS-*b*-P4VP overlayers could be due to increased hydrophobicity from the PS groups.

Recent work by Koper et al. reported a correlation between formate activity at low overpotentials and a decrease in proton transport.¹³ It was hypothesized that the regulation of proton and water transport originated from increased hydrophobicity induced by a P4VP coating on a Cu electrode. They used contact angle measurements with water to gauge the degree of hydrophobicity induced via P4VP. Following a similar framework, contact angle measurements were performed on the polymer overlayers alongside the unmodified Ag. The unmodified Ag exhibited the highest contact angle of ≈97° (Figure 3), albeit the trace volatile carbons from the ambient could (Figure S1b,c) influence this observation. Introducing 6 nm of P4VP onto the Ag surface increases the hydrophilicity, where the coated electrode exhibits a contact angle near 51.2°,

while the thicker 34 nm P4VP layer (not shown) exhibits a slightly lower contact angle of 45.7° and 6 nm PS results in a contact angle of 89.2°. Intriguingly, the block copolymer behaves in between the two extremes with contact angles of 57.9 and 85° for the 40k PS-*b*-P4VP and 10k PS-*b*-P4VP, respectively, which could suggest a hierarchical domain ordering within the film such that 40k PS-*b*-P4VP has more P4VP groups at the air interface, while 10k PS-*b*-P4VP has more PS. The Wenzel equation (eq 7) was applied to evaluate the impact of roughness on the measured contact angles, where θ_m is the measured contact angle, R is the roughness ratio (Table S3), and θ_y is the Young contact angle. For the roughest polymer layer (40k PS-*b*-P4VP at $R = 1.008$), the measured contact angle is 57.9°, while the calculated Young contact angle is only 0.3° larger at 58.2°.⁴⁸ Therefore, it was concluded that the roughness of the polymer film played a negligible role in the contact angle measurements.

$$\cos(\theta_m) = R \cos(\theta_y) \quad (7)$$

The hydrophobicity of PS hardly comes as a surprise as it is widely accepted to be impermeable to aqueous solutions only taking up 0.17% of H₂O.⁴⁹ Given the inert hydrocarbon backbone, its nonpolar nature has no chemical driving force to interact with H₂O. That said, it is intriguing that the HER, which requires either protons (which can be provided through HCO₃[−] transport)^{34,50–53} or H₂O, still occurs at appreciable rates for the electrodes covered with smooth layers of PS. One possible explanation for this could be defects that result in pores containing the electrolyte, which enable the migration of aqueous species to the electrode surface. However, this would be limited to pore sizes that still obstruct the transport of CO₂ attenuating the local CO₂ concentration. Another contributing factor could be the permeability of water vapor through polystyrene, which is notable.⁵⁴ An alternative mechanism could be that the polymer layer screens cations from the surface, which stabilize the CO₂[−] intermediate. Scanning electrochemical microscopy observed that the conversion of CO₂ to CO was only observed in the presence of cations.⁵⁵ Either mechanism could explain the higher activity and selectivity for HER. In the case of P4VP, the increased activity toward CO could be explained as a combination of the electronic modification to the Ag active sites, which has been observed in the recent literature and possibly modified transport properties of CO₂ and protons through the layer of

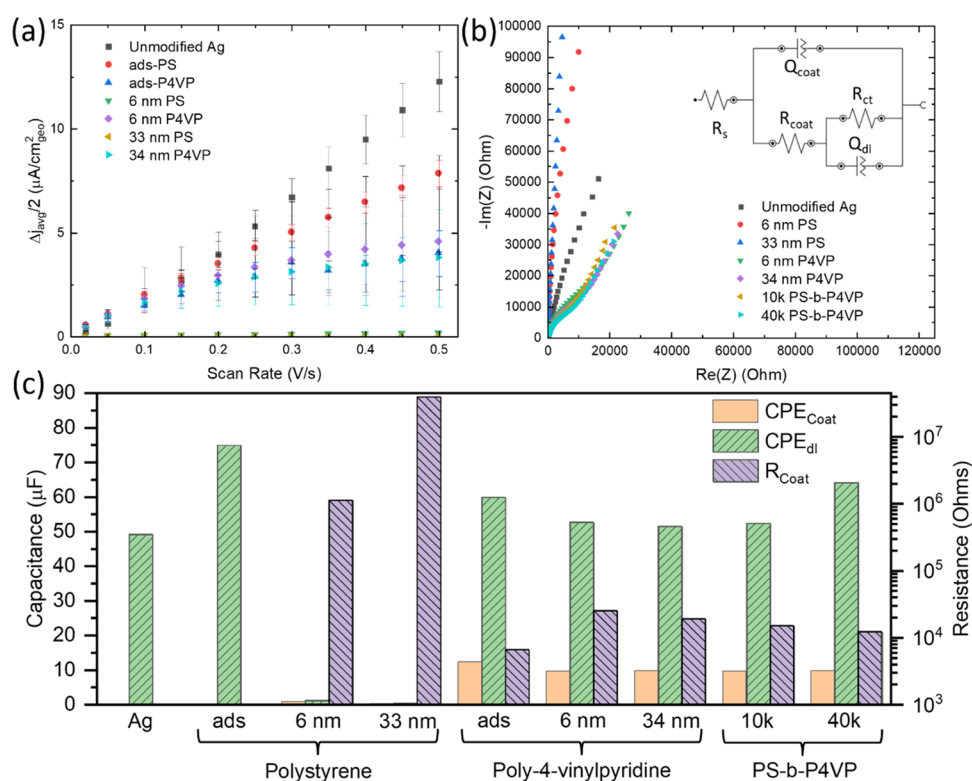


Figure 4. (a) Double layer currents (determined by averaging the current between 0.62 and 0.68 V) vs scan rate and (b) EIS at 0.58 V of Ag with polymer overlayers. (c) Results of fitting (circuit presented in the inset of (b)) EIS data. A simple R - R // Q was used for Ag.

pyridine groups.⁸ Given that the 10k and 40k PS-*b*-P4VP overlayer electrodes had contact angles between the two extremes, it is logical that the combination of Ag–pyridine interactions and modified transport phenomena contribute to the observed catalytic output.

Double layer capacitance (DLC) (Figures S17 and S18) and electrochemical impedance were measured in a nonfaradaic potential window between 0.59 and 0.71 V (Figure 4), where the average current was determined by averaging between 0.62 and 0.68 V in Ar-saturated 0.1 mol L⁻¹ KHCO₃ (see the Methods section) to further evaluate the influence of PS, P4VP, and PS-*b*-P4VP overlayers on charge transport. Ag electrodes with adsorbed layers of PS and P4VP (Figure S17a,b) show response akin to that of unmodified Ag (Figure S4a), with the exception that the Ag with ads-P4VP shows more shear in the voltammetric response. The measured DLC curves (Figure 4a) depict a lower linear slope for ads-PS compared to the unmodified Ag and a nonlinear behavior for Ag with ads-P4VP. The nonlinear behavior indicates nonideal double layer behavior, indicating that the transport of ions through the film is slower. Thicker overlayers of P4VP on Ag (Figure S17e,f) maintained similar behavior in capacitance but with more extreme shearing in the voltammetric response at higher scan rates. In fact, all P4VP and PS-*b*-P4VP overlayer electrodes show behavior similar to the unmodified Ag at slow scan rates but have lower DLC current at faster scan rates. On the other hand, thicker layers of PS suppressed any capacitive response to potential sweeps by orders of magnitude, scaling with thickness (Figure S17b,c). For example, Ag with ads-PS produced a capacitance of 15.7 $\mu\text{F cm}^{-2}$, Ag with 6 nm PS produced a capacitance of 0.3 $\mu\text{F cm}^{-2}$, and Ag with 33 nm PS was statistically unmeasurable, a capacitance <1 nF cm⁻². Both 10k and 40k PS-*b*-P4VP overlayers yield similar DLC values to

P4VP regarding capacitive behavior (Figure S18). These results suggest a complete impediment of ion transport through the PS layer, while the response on P4VP suggests partial mitigation of ion transport. It should be noted that the DLC (and EIS discussed below) and CO₂ reduction measurements could influence the state of the polymer films differently. Bubble generation from the HER could cause changes in film thickness or even result in delamination, whereas the DLC measurements are conducted in the absence of faradaic reactions; thus, the polymer film is less perturbed over the course of the measurement. These differences could explain the absence of ion transport in the case of DLC measurements.

Nyquist plots from EIS collected at 0.58 V (see the Methods section for more details) portray the stark difference between PS overlayers and pyridine-containing polymers (both P4VP and PS-*b*-P4VP). Ag electrodes with PS overlayers exhibit a much larger imaginary impedance compared to unmodified Ag, while P4VP overlayers display the opposite effect. A simple R_s - R_{ct} // CPE_{dl} circuit was used for Ag, where R_s signifies solution resistance, R_{ct} is the charge-transfer resistance, and CPE_{dl} models the double layer capacitance using a constant phase element. The circuit developed to model impedance of the polymer-coated electrodes (Figure 4b, inset) expands upon this basis, adding in an R_{coat} // CPE_{coat} element to account for impedance of the polymer coating. Similar circuit models are used to characterize organic coatings on metal electrodes.⁵⁶

The fitting results from EIS measurements are summarized in Figure 4c. Coatings of PS thicker than just the adsorbed layer resulted in a completely diminished CPE_{dl} , consistent with our results from the DLC experiments, as well as results from other reports.⁵⁷ The other coated electrodes (P4VP and PS-*b*-P4VP) maintain CPE_{dl} values on par with the unmodified

Ag electrode, demonstrating accessibility of the electrolyte to the metal surface. Addition of the 6 nm layer of PS resulted in an R_{coat} of roughly 1 M Ω , while increasing the thickness to 33 nm of PS increased the resistance to nearly 40 M Ω , significantly higher than the other coatings. Furthermore, the PS-coated electrodes did not demonstrate a significant coating capacitance given its lack of charge carriers. These EIS results for PS confirm the extreme obstruction of electrolyte species transport through the PS layer to the electrode surface.

In contrast, EIS results from P4VP and PS-*b*-P4VP-coated electrodes demonstrate much lower R_{coat} on the order of 10 k Ω , and CPE_{coat} near 10 μF (or 5 $\mu\text{F cm}^{-2}$). R_{coat} is higher in the thicker P4VP films compared to the ads-P4VP sample but remain fairly constant with increasing layer thickness. Connecting EIS to electrolysis experiments, the pyridine-containing polymer overlayers inhibit ion transport (presumably protons and (bi)carbonate) to the electrode surface that leads to diminished HER activity. Going further, the CPE_{dl} of each electrode composite serves as a numeric for the electrochemically active surface area (ECSA), assuming a standard capacitance of 25 $\mu\text{F/cm}^2$ for Ag.⁵⁷ This enables the comparison of eCO₂RR activity for electrodes with P4VP and PS-*b*-P4VP overlayers (Figure S19). While the general trends observed based on geometric current densities remain to be true, it appears in the case of PS-*b*-P4VP overlayers that the specific CO current density is almost the same for both block copolymer sizes (Figure S19b). However, the specific H₂ current density is lower for the larger block. This suggests that the larger block size, rather than enhancing eCO₂RR activity, attenuates HER likely through substrate transport to the surface. However, the similarity in EIS between P4VP and PS-*b*-P4VP coatings suggests that the structural conformation PS-*b*-P4VP at the metal electrode does not impede ionic transport to the surface any more than P4VP even though contact angle measurements point to a slightly higher hydrophobicity of the electrolyte/polymer interface. Further investigation into the specific polymeric structures resulting from the different block sizes could enable better understanding of the observed catalytic differences. Both EIS and DLC measurements are consistent with the observations that thicker PS layers severely inhibit electrochemical activity at the Ag surface, while pyridine-containing overlayers (either in block co- or homopolymers) preserve accessibility.

CONCLUSIONS

This investigation explored the effects of polymer overlayers on the eCO₂RR at a textured Ag(111) surface. It was demonstrated that the functional groups along a polyvinyl backbone significantly impact the catalytic properties of the metal surface. In the case of polystyrene, the eCO₂RR was fully suppressed with a 6 nm polymer layer and the hydrogen evolution reaction was enhanced 3 \times , likely a side effect of blocking CO₂ from reaching the surface and converting to surface-adsorbed CO. Substituting a pyridine group for the benzene ring in polystyrene had the inverse effect; it substantially enhanced the rate of CO₂ conversion to CO while suppressing the hydrogen evolution reaction. Interestingly, block copolymers consisting of both PS and P4VP segments show minor dependence on block size, with larger blocks (20k–20k) having slightly higher selectivity toward CO than the P4VP homopolymer and shorter blocks (5k–5k) having lower selectivity compared to P4VP-covered electrodes. These differences suggest that hierarchical overlayer structures

at and extending from the electrode surface play a role in controlling reaction selectivity. Contact angle measurements, XPS, and EIS investigations suggest that hydrophobicity, chemical modification, and ion transport all played a role in the observed catalytic activity. Future *in situ* measurements that characterize the structural conformations of these polymers, among others, and transport of species through them could provide further insight into the desired properties of metal–polymer composite electrodes for the electrochemical conversion of CO₂. This study demonstrates the importance of understanding both the chemical and physical makeups, including larger length-scale conformations, of polymeric additives used in electrocatalytic reactions.

ASSOCIATED CONTENT

Supporting Information

The Supporting Information is available free of charge at <https://pubs.acs.org/doi/10.1021/acs.jpcc.3c03157>.

Detailed discussion of XRD and XRR measurements; bare Ag thin film surface characterization via XPS, AFM, and DLC measurements; control ellipsometry measurements for Ag and polymer thin film constants; AFM images of Ag thin films and Ag thin films with polymer overlayers; RMS roughness of the Ag thin film and Ag thin films with polymer overlayers; XPS spectra of Ag thin films with PS and P4VP overlayers; standard XPS of bulk PS and P4VP; XPS of Ag thin films with 10k and 40k PS-*b*-P4VP overlayers; faradaic efficiencies for H₂ and CO, and current density for eCO₂RR experiments on Ag thin films and Ag thin films with polymer overlayers; partial current density for formate on Ag thin films and Ag thin films with polymer overlayers; eCO₂RR activity comparison between potential steps for the Ag thin film; N content comparison before and after electrochemistry for Ag thin films with P4VP overlayers; cyclic voltammetry for DLC measurements of Ag thin films and Ag thin films with polymer overlayers; DLC results comparing Ag thin films with P4VP, 10k, and 40k PS-*b*-P4VP overlayers (PDF)

AUTHOR INFORMATION

Corresponding Author

David Raciti – Materials Science and Engineering Division, National Institute of Standards and Technology, Gaithersburg, Maryland 20899, United States; orcid.org/0000-0002-9580-4524; Email: david.raciti@nist.gov

Authors

Ally Guo – Materials Science and Engineering Division, National Institute of Standards and Technology, Gaithersburg, Maryland 20899, United States

Avery E. Baumann – Materials Science and Engineering Division, National Institute of Standards and Technology, Gaithersburg, Maryland 20899, United States; orcid.org/0000-0001-8513-8049

Eric D. Rus – Materials Science and Engineering Division, National Institute of Standards and Technology, Gaithersburg, Maryland 20899, United States; orcid.org/0000-0001-5031-6888

Christopher M. Stafford – Materials Science and Engineering Division, National Institute of Standards and Technology,

Gaithersburg, Maryland 20899, United States; orcid.org/0000-0002-9362-8707

Complete contact information is available at:
<https://pubs.acs.org/10.1021/acs.jpcc.3c03157>

Notes

*Certain commercial equipment, instruments, or materials are identified in this paper to specify the experimental procedure adequately. Such an identification is not intended to imply recommendation or endorsement by the National Institute of Standards and Technology, nor is it intended to imply that the materials or equipment identified are necessarily the best available for the purpose.

The authors declare no competing financial interest.

ACKNOWLEDGMENTS

The authors would like to thank Gery Stafford for his guidance in electrochemical impedance spectroscopy analysis and fitting.

REFERENCES

- (1) Shukla, P. R.; Skea, J.; Slade, R.; Al Khourdajie, A.; van Diemen, R.; McCollum, D.; Pathak, M.; Some, S.; Vyas, P.; Fradera, M. et al. *Climate Change 2022: Mitigation of Climate Change. Working Group III Contribution to the IPCC Sixth Assessment Report*; U.K. and New York, NY, USA.
- (2) Nitopi, S.; Bertheussen, E.; Scott, S. B.; Liu, X.; Engstfeld, A. K.; Horch, S.; Seger, B.; Stephens, I. E. L.; Chan, K.; Hahn, C.; et al. Progress and Perspectives of Electrochemical CO₂ Reduction on Copper in Aqueous Electrolyte. *Chem. Rev.* **2019**, *119*, 7610–7672.
- (3) Raciti, D.; Wang, C. Recent Advances in CO₂ Reduction Electrocatalysis on Copper. *ACS Energy Lett.* **2018**, *3*, 1545–1556.
- (4) Wang, Y.; Shen, H.; Livi, K. J. T.; Raciti, D.; Zong, H.; Gregg, J.; Onadoko, M.; Wan, Y.; Watson, A.; Wang, C. Copper Nanocubes for CO₂ Reduction in Gas Diffusion Electrodes. *Nano Lett.* **2019**, *19*, 8461–8468.
- (5) Zhao, S.; Jin, R.; Jin, R. Opportunities and Challenges in CO₂ Reduction by Gold- and Silver-Based Electrocatalysts: From Bulk Metals to Nanoparticles and Atomically Precise Nanoclusters. *ACS Energy Lett.* **2018**, *3*, 452–462.
- (6) Banerjee, S.; Zhang, Z.-Q.; Hall, A. S.; Thoi, V. S. Surfactant Perturbation of Cation Interactions at the Electrode–Electrolyte Interface in Carbon Dioxide Reduction. *ACS Catal.* **2020**, *10*, 9907–9914.
- (7) Hu, H.; Liu, M.; Kong, Y.; Mysuru, N.; Sun, C.; Gálvez-Vázquez, M. d. J.; Müller, U.; Erni, R.; Grozovski, V.; Hou, Y.; Broekmann, P. Activation Matters: Hysteresis Effects during Electrochemical Looping of Colloidal Ag Nanowire Catalysts. *ACS Catal.* **2020**, *10*, 8503–8514.
- (8) Abdinejad, M.; Irtem, E.; Farzi, A.; Sassenburg, M.; Subramanian, S.; Iglesias van Montfort, H.-P.; Ripepi, D.; Li, M.; Middelkoop, J.; Seifitokaldani, A.; Burdyny, T. CO₂ Electrolysis via Surface-Engineering Electrografted Pyridines on Silver Catalysts. *ACS Catal.* **2022**, *12*, 7862–7876.
- (9) Tapan, N. A. CO₂ Electroreduction on P4VP Modified Copper Deposited Gas Diffusion Layer Electrode: PH Effect. *Mater. Renewable Sustainable Energy* **2016**, *5*, No. 19.
- (10) Li, F.; Tang, Q. Understanding the Role of Functional Groups of Thiolate Ligands in Electrochemical CO₂ Reduction over Au(111) from First-Principles. *J. Mater. Chem. A* **2019**, *7*, 19872–19880.
- (11) Zhang, Z.-Q.; Banerjee, S.; Thoi, V. S.; Shoji Hall, A. Reorganization of Interfacial Water by an Amphiphilic Cationic Surfactant Promotes CO₂ Reduction. *J. Phys. Chem. Lett.* **2020**, *11*, 5457–5463.
- (12) Chernyshova, I. V.; Somasundaran, P.; Ponnuram, S. On the Origin of the Elusive First Intermediate of CO₂ Electroreduction. *Proc. Natl. Acad. Sci. U.S.A.* **2018**, *115*, E9261–E9270.
- (13) Ye, C.; Raaijman, S. J.; Chen, X.; Koper, M. T. M. Enhanced Electrochemical CO₂ Reduction to Formate on Poly(4-Vinylpyridine)-Modified Copper and Gold Electrodes. *ACS Appl. Mater. Interfaces* **2022**, *14*, 45263–45271.
- (14) Nam, D.-H.; De Luna, P.; Rosas-Hernández, A.; Thevenon, A.; Li, F.; Agapie, T.; Peters, J. C.; Shekha, O.; Eddaoudi, M.; Sargent, E. H. Molecular Enhancement of Heterogeneous CO₂ Reduction. *Nat. Mater.* **2020**, *19*, 266–276.
- (15) Han, Z.; Kortlever, R.; Chen, H.-Y.; Peters, J. C.; Agapie, T. CO₂ Reduction Selective for C₂ Products on Polycrystalline Copper with N-Substituted Pyridinium Additives. *ACS Cent. Sci.* **2017**, *3*, 853–859.
- (16) Xie, M. S.; Xia, B. Y.; Li, Y.; Yan, Y.; Yang, Y.; Sun, Q.; Chan, S. H.; Fisher, A.; Wang, X. Amino Acid Modified Copper Electrodes for the Enhanced Selective Electroreduction of Carbon Dioxide towards Hydrocarbons. *Energy Environ. Sci.* **2016**, *9*, 1687–1695.
- (17) Chen, X.; Chen, J.; Alghoraibi, N. M.; Henckel, D. A.; Zhang, R.; Nwabara, U. O.; Madsen, K. E.; Kenis, P. J. A.; Zimmerman, S. C.; Gewirth, A. A. Electrochemical CO₂-to-Ethylene Conversion on Polyamine-Incorporated Cu Electrodes. *Nat. Catal.* **2021**, *4*, 20–27.
- (18) Luo, M.; Ozden, A.; Wang, Z.; Li, F.; Erick Huang, J.; Hung, S.-F.; Wang, Y.; Li, J.; Nam, D.-H.; Li, Y. C.; et al. Coordination Polymer Electrocatalysts Enable Efficient CO-to-Acetate Conversion. *Adv. Mater.* **2023**, *35*, No. 2209567.
- (19) Thevenon, A.; Rosas-Hernández, A.; Peters, J. C.; Agapie, T. In-Situ Nanostructuring and Stabilization of Polycrystalline Copper by an Organic Salt Additive Promotes Electrocatalytic CO₂ Reduction to Ethylene. *Angew. Chem., Int. Ed.* **2019**, *58*, 16952–16958.
- (20) Li, F.; Thevenon, A.; Rosas-Hernández, A.; Wang, Z.; Li, Y.; Gabardo, C. M.; Ozden, A.; Dinh, C. T.; Li, J.; Wang, Y.; et al. Molecular Tuning of CO₂-to-Ethylene Conversion. *Nature* **2020**, *577*, 509–513.
- (21) Zhang, J.; Deo, S.; Janik, M. J.; Medlin, J. W. Control of Molecular Bonding Strength on Metal Catalysts with Organic Monolayers for CO₂ Reduction. *J. Am. Chem. Soc.* **2020**, *142*, 5184–5193.
- (22) Buckley, A. K.; Cheng, T.; Oh, M. H.; Su, G. M.; Garrison, J.; Utan, S. W.; Zhu, C.; Toste, F. D.; Goddard, W. A.; Toma, F. M. Approaching 100% Selectivity at Low Potential on Ag for Electrochemical CO₂ Reduction to CO Using a Surface Additive. *ACS Catal.* **2021**, *11*, 9034–9042.
- (23) Wakerley, D.; Lamaison, S.; Ozanam, F.; Menguy, N.; Mercier, D.; Marcus, P.; Fontecave, M.; Mougél, V. Bio-Inspired Hydrophobicity Promotes CO₂ Reduction on a Cu Surface. *Nat. Mater.* **2019**, *18*, 1222–1227.
- (24) Seshadri, G.; Lin, C.; Bocarsly, A. B. A New Homogeneous Electrocatalyst for the Reduction of Carbon Dioxide to Methanol at Low Overpotential. *J. Electroanal. Chem.* **1994**, *372*, 145–150.
- (25) Lucio, A. J.; Shaw, S. K. Pyridine and Pyridinium Electrochemistry on Polycrystalline Gold Electrodes and Implications for CO₂ Reduction. *J. Phys. Chem. C* **2015**, *119*, 12523–12530.
- (26) De Riccardis, A.; Lee, M.; Kazantsev, R. V.; Garza, A. J.; Zeng, G.; Larson, D. M.; Clark, E. L.; Lobaccaro, P.; Burroughs, P. W. W.; Bloise, E.; et al. Heterogenized Pyridine-Substituted Cobalt(II) Phthalocyanine Yields Reduction of CO₂ by Tuning the Electron Affinity of the Co Center. *ACS Appl. Mater. Interfaces* **2020**, *12*, 5251–5258.
- (27) Messias, I.; Pinto, M. R.; Roveda, A. C.; Queiroz, A. C.; Lima, F. H. B.; Nagao, R. Electrochemical Mass Spectrometry Study of the Pyridine/Pyridinium in the CO₂ Electroreduction Reaction on Copper Electrodes. *Electrochim. Acta* **2022**, *436*, No. 141445.
- (28) Yang, H.-P.; Qin, S.; Yue, Y.-N.; Liu, L.; Wang, H.; Lu, J.-X. Entrapment of a Pyridine Derivative within a Copper–Palladium Alloy: A Bifunctional Catalyst for Electrochemical Reduction of CO₂ to Alcohols with Excellent Selectivity and Reusability. *Catal. Sci. Technol.* **2016**, *6*, 6490–6494.
- (29) Lebègue, E.; Agullo, J.; Morin, M.; Bélanger, D. The Role of Surface Hydrogen Atoms in the Electrochemical Reduction of

Pyridine and CO₂ in Aqueous Electrolyte. *ChemElectroChem* **2014**, *1*, 1013–1017.

(30) Lim, C.-H.; Holder, A. M.; Musgrave, C. B. Mechanism of Homogeneous Reduction of CO₂ by Pyridine: Proton Relay in Aqueous Solvent and Aromatic Stabilization. *J. Am. Chem. Soc.* **2013**, *135*, 142–154.

(31) Jeong, H.; Kang, M. J.; Jung, H.; Kang, Y. S. Electrochemical CO₂ Reduction with Low Overpotential by a Poly(4-Vinylpyridine) Electrode for Application to Artificial Photosynthesis. *Faraday Discuss.* **2017**, *198*, 409–418.

(32) Raciti, D.; Livi, K. J.; Wang, C. Highly Dense Cu Nanowires for Low-Overpotential CO₂ Reduction. *Nano Lett.* **2015**, *15*, 6829–6835.

(33) Raciti, D.; Cao, L.; Livi, K. J. T.; Rottmann, P. F.; Tang, X.; Li, C.; Hicks, Z.; Bowen, K. H.; Hemker, K. J.; Mueller, T.; Wang, C. Low-Overpotential Electroreduction of Carbon Monoxide Using Copper Nanowires. *ACS Catal.* **2017**, *7*, 4467–4472.

(34) Raciti, D.; Braun, T.; Tackett, B. M.; Xu, H.; Cruz, M.; Wiley, B. J.; Moffat, T. P. High-Aspect-Ratio Ag Nanowire Mat Electrodes for Electrochemical CO Production from CO₂. *ACS Catal.* **2021**, *11*, 11945–11959.

(35) Akbari, R.; Antonini, C. Contact Angle Measurements: From Existing Methods to an Open-Source Tool. *Adv. Colloid Interface Sci.* **2021**, *294*, No. 102470.

(36) Bondarenko, A. S.; Ragoisha, G. A. Progress in Chemometrics Research. *Nova Sci. Pub.* **2005**, 89–102.

(37) Kennemur, J. G. Poly(Vinylpyridine) Segments in Block Copolymers: Synthesis, Self-Assembly, and Versatility. *Macromolecules* **2019**, *52*, 1354–1370.

(38) Girardeaux, C.; Pireaux, J.-J. Analysis of Polystyrene (PS) by XPS. *Surf. Sci. Spectra* **1996**, *4*, 130–133.

(39) XPS of Polymers Database, Surface Spectra. <https://surfacespectra.com/xps/> (accessed 2023-04-02).

(40) Eesley, G. L.; Burkstrand, J. M. X-Ray-Photoemission and Raman Spectroscopy Investigation of Pyridine on Ag. *Phys. Rev. B* **1981**, *24*, 582–585.

(41) Dolatkah, A.; Jani, P.; Wilson, L. D. Redox-Responsive Polymer Template as an Advanced Multifunctional Catalyst Support for Silver Nanoparticles. *Langmuir* **2018**, *34*, 10560–10568.

(42) Ferrara, A. M.; Carapeto, A. P.; Botelho do Rego, A. M. X-Ray Photoelectron Spectroscopy: Silver Salts Revisited. *Vacuum* **2012**, *86*, 1988–1991.

(43) Hoshi, N.; Kato, M.; Hori, Y. Electrochemical Reduction of CO₂ on Single Crystal Electrodes of Silver Ag(111), Ag(100) and Ag(110). *J. Electroanal. Chem.* **1997**, *440*, 283–286.

(44) Clark, E. L.; Ringe, S.; Tang, M.; Walton, A.; Hahn, C.; Jaramillo, T. F.; Chan, K.; Bell, A. T. Influence of Atomic Surface Structure on the Activity of Ag for the Electrochemical Reduction of CO₂ to CO. *ACS Catal.* **2019**, *9*, 4006–4014.

(45) Chason, E. A Kinetic Analysis of Residual Stress Evolution in Polycrystalline Thin Films. *Thin Solid Films* **2012**, *526*, 1–14.

(46) Chason, E.; Engwall, A. M. Relating Residual Stress to Thin Film Growth Processes via a Kinetic Model and Real-Time Experiments. *Thin Solid Films* **2015**, *596*, 2–7.

(47) Rao, Z.; Berman, S.; Yang, P.; Depla, D.; Chason, E. Understanding Residual Stress in Thin Films: Analyzing Wafer Curvature Measurements for Ag, Cu, Ni, Fe, Ti, and Cr with a Kinetic Model. *J. Appl. Phys.* **2021**, *130*, No. 135304.

(48) Wenzel, R. N. Resistance of Solid Surfaces to Wetting by Water. *Ind. Eng. Chem.* **1936**, *28*, 988–994.

(49) Cheng, J.; Chen, Z.; Zhou, J.; Cao, Z.; Wu, D.; Liu, C.; Pu, H. Influences of Layer Thickness on the Compatibility and Physical Properties of Polycarbonate/Polystyrene Multilayered Film via Nanolayer Coextrusion. *Appl. Surf. Sci.* **2018**, *440*, 946–954.

(50) Raciti, D.; Mao, M.; Wang, C. Mass Transport Modelling for the Electroreduction of CO₂ on Cu Nanowires. *Nanotechnology* **2018**, *29*, No. 044001.

(51) Dunwell, M.; Lu, Q.; Heyes, J. M.; Rosen, J.; Chen, J. G.; Yan, Y.; Jiao, F.; Xu, B. The Central Role of Bicarbonate in the

Electrochemical Reduction of Carbon Dioxide on Gold. *J. Am. Chem. Soc.* **2017**, *139*, 3774–3783.

(52) Dunwell, M.; Yang, X.; Setzler, B. P.; Anibal, J.; Yan, Y.; Xu, B. Examination of Near-Electrode Concentration Gradients and Kinetic Impacts on the Electrochemical Reduction of CO₂ Using Surface-Enhanced Infrared Spectroscopy. *ACS Catal.* **2018**, *8*, 3999–4008.

(53) Chen, Y.; Li, C. W.; Kanan, M. W. Aqueous CO₂ Reduction at Very Low Overpotential on Oxide-Derived Au Nanoparticles. *J. Am. Chem. Soc.* **2012**, *134*, 19969–19972.

(54) Mánik, M.; Medved, I. Transmission of Water Vapor through Expanded Polystyrene. *AIP Conf. Proc.* **2020**, *2275*, No. 020020.

(55) Monteiro, M. C. O.; Dattila, F.; Hagedoorn, B.; García-Muelas, R.; López, N.; Koper, M. T. M. Absence of CO₂ Electroreduction on Copper, Gold and Silver Electrodes without Metal Cations in Solution. *Nat. Catal.* **2021**, *4*, 654–662.

(56) Cesiulis, H.; Tsyntaru, N.; Ramanavicius, A.; Ragoisha, G. The Study of Thin Films by Electrochemical Impedance Spectroscopy. In *Nanostructures and Thin Films for Multifunctional Applications*; Tiginyanu, I.; Topala, P.; Ursaki, V., Eds.; NanoScience and Technology; Springer International Publishing: Cham, 2016; pp 3–42. DOI: 10.1007/978-3-319-30198-3_1.

(57) Yoon, Y.; Hall, A. S.; Surendranath, Y. Tuning of Silver Catalyst Mesostructure Promotes Selective Carbon Dioxide Conversion into Fuels. *Angew. Chem., Int. Ed.* **2016**, *55*, 15282–15286.

Recommended by ACS

CO₂RR-to-CO Enhanced by Self-Assembled Monolayer and Ag Catalytic Interface

Zhengyang Yang, Fanglin Che, *et al.*

SEPTEMBER 06, 2023

THE JOURNAL OF PHYSICAL CHEMISTRY C

READ 

Breaking the Limit of Size-Dependent CO₂RR Selectivity in Silver Nanoparticle Electrocatalysts through Electronic Metal–Carbon Interactions

Xingyi Deng, Douglas R. Kauffman, *et al.*

NOVEMBER 10, 2023

ACS CATALYSIS

READ 

Dynamic Metal–Ligand Coordination Boosts CO₂ Electroreduction

Xiangdong Kong, Zhigang Geng, *et al.*

JUNE 13, 2023

JOURNAL OF THE AMERICAN CHEMICAL SOCIETY

READ 

A Bifunctional Ionic Liquid for Capture and Electrochemical Conversion of CO₂ to CO over Silver

Saudagar Dongare, Burcu Gurkan, *et al.*

MAY 25, 2023

ACS CATALYSIS

READ 

Get More Suggestions >